16

High-Speed, High-Power, and High Responsivity Photodiode for Radio-Over-Fiber (ROF) Communication

J.-W. Shi, F.-M. Kuo and Y.-S. Wu
Department of Electrical Engineering, National Central University
Taiwan

1. Introduction

The tremendous increase in the required volume of wireless data-transmission has stimulated attention on ways to use the millimeter wave (MMW) bands above 60GHz (V-band) or above 100GHz (W-band) as the carrier frequency for the realization of systems with very high transmission data rates in excess of many gigabits-per-second [1,2]. Unfortunately, there is a large propagation loss of the MMW signal in the >W-band or V-band frequencies, whether in free space or in a coaxial cable. One promising solution to this problem is the radio-over-fiber (ROF) technique [1-3], where the MMW signal is distributed through a lossless optical fiber and then radiated over the last-mile to the user-end. High-speed, high responsivity, and high-power photodiodes (PD) serve as a key component in photonic MMW communication systems [1] for transducing the intense optical power to high-power MMW power. The saturation current-bandwidth product is thus a key parameter for evaluating the performance of high-power photodiodes (PD) for such applications, especially when the operating frequency is around 100GHz or higher. By increasing the saturation current of the PD, we can boost the injected optical power and further increase the maximum available MMW power. The burden imposed on the MMW power amplifier can thus be relaxed [4,5]. Recently, a research group at NTT reported excellent results for a 10Gb/s wireless link at 120GHz, achieved by using a high-power uni-traveling-carrier photodiode (UTC-PD) based photonic transmitter [1,2].

There are two approaches to improve the high-power performance of PDs. One is to distribute and uniform the photocurrents along the edge-coupled PDs to minimize the thermal problem [6] and space-charge screening effect [4,5] by improving the geometric structure of optical and electrical waveguides, such as, evanescently-coupled photodiode (ECPD) [7-9]; the other is to minimize the space-charge screening effect in the photo-absorption volume by changing the structure or material of epitaxial layers, such as UTC-PD [4,5], partially depleted absorber photodiode (PDP) [10], and separated-transport-recombination photodiode (STR-PD) [11]. In this chapter, we reviewed our recent works on InP and GaAs based high-power photodiodes, which can overcome the above-mentioned problems and achieve state-of-the-art output power without seriously sacrificing the

responsivity and speed performance.

2. Geometric Structure of High-power, High-responsivity, and High-speed Photodiode

2.1 Introduction

Figure 1 (a) and (b) shows the cross-sectional view of vertical-illuminated PDs (VPD) and WGPD, respectively. Compared with the structure of typical VPDs, the structure of the edge-coupled waveguide photodiode WGPD [4] has attracted a lot of attention due to its superior bandwidth-responsivity product performance [4]. In VPDs strcuture, the direction of carrier transport is parallel with the direction of incident photon and in order to shorten the carrier drift-time inside the absorption regime, we must decrease the absorption layer thickenss and the reponsivity performance will thus be sacrifieced for high-speed perfroamnce. On the other hand, in WGPD structure, the direction of carrier transport is perpicdular to the direction of incident photon and we can still use a thin absorption layer (<200nm) to absorb the edge-coupling photon completely by using a proper length of active waveguide, however, its maximum output photocurrent is seriously limited, due to the problem of saturation at the input-end of device [4]. Figure 2 shows the conceptual diagram of input-end-satutaion problem in WGPD. As can be seen, most of the incident photon will be absorbed near the input-end of WGPD and the high density of photo-generated carriers would thus saturate the device output power. There are two major trends being followed to improve the high-power performance of the WGPD. One is to distribute and make uniform the photocurrents by improving the structure of optical and electrical waveguides, such as research into the velocity matched distributed photodetector (VMDP) [12] and the other is evanescently-coupled photodiode (ECPD) [7-9]. As can be seen in Figure 2, the incident photon is launched to the bottom passive optical waveguide of ECPD and gradually coupled to the upper active absorption region. Becasue the gradually coupling process into the absorption regime, the distribution of photo-generated carriers thus becoems more uniform and the problem of input-end saturation in traditional WGPD can thus be minimized. Recently, several research groups have demonstrated the state-of-the-art performance of ECPDs with a short coupling length (~20μm) and partially depleted absorber [8,9]. However, the tolerance of the cleaved coupling length of such devices is very small (less than 5μm) and different coupling lengths have a serious effect on the responsivity performance [8]. This problem can be overcome by dry etching a deep trench to precisely define the waveguide length [13]. However, any roughness on the dry-etched

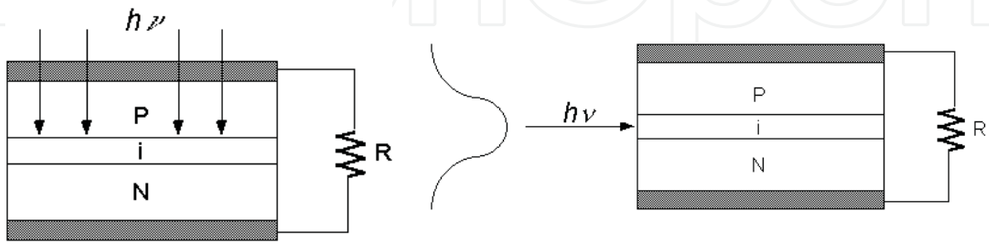

Fig. 1. Schematic diagram of a p-i-n based VPD (a) and WGPD (b) structure.

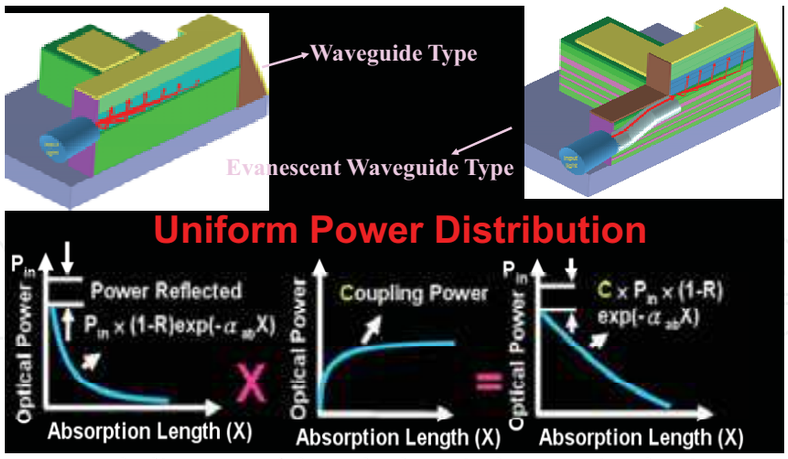

Fig. 2. The conceptual diagram of launched optical wave in the input-end of WGPD structure and ECPD structure

facets can degrade the responsivity performance. Other groups have also developed photodiodes with an asymmetric twin waveguide (tapered) structure to improve the cleaving tolerance and achieve high responsivity performance [7] but the misalignment between these twin waveguides and the optical scattering loss, which is induced by very long waveguide lengths (>700μm), can both seriously affect the responsivity [7]. In additiom, by integrating an edge-coupled PD with a leaky optical waveguide, is another possible soulution to increase the tolerance of the cleaving process [12], although the electrical bandwidth performance may be sacrificed for the high responsivity performance, due to the fact that a much larger photo-absorption volume than that of the traditional WGPD is necessary to completely absorb the diluted optical power [4,12]. In this chapter, we reviewed our recent works [14,15], which can overcome the abvoe-mentioned problems of ECPD and achieve the goal of high-bandwdith, high-responsivity, and high saturation power. At first, we combined a partially p-doped photo-absorption layer with a leaky optical waveguide and a distributed-bragg-reflector (DBR) in the structure of an edge-coupled photodiode. The integrated DBR mirror can fold the injected optical path and enhance the responsivity performance without increasing the device-absorption-length. The demonstrated device can achieve superior performance in terms of bandwidth, saturation power, and quantum efficiency for the control, without DBR mirrors. Furthermore, the responsivity performance of our demonstrated device is much less sensitive to the cleaved coupling length than is that that of the ECPD (7% vs. 30% [8]). The another structure we demonstarted for solving the problems of ECPD is the dual-step evanescently-coupled waveguide photodiode [15] (DECPD). By separating the fiber-guide region and coupling-guide region into different parts of the optical waveguide [15], the dependence of the responsivity on the cleaved-length can be minimized, nor is a long (~700μm) passive waveguide with complex tapered stages any longer necessary.

2.2 Leaky-Waveguide PDs

In order to determine the influence of DBR mirrors on the responsivity performance of photodiodes, two kinds of device, with the same geometry and epi-layer structures, but with and without DBR mirrors, were fabricated. The DBR mirror device has twice the reflected input optical power and absorption of the folded optical power. Thus, compared with the DBR device, the control device requires a much longer device-absorption-length, which results in poorer speed performance. The cross-sectional view and top-view of the demonstrated devices are given in Figure 3 and the inset shows the fabricated DBR mirror.

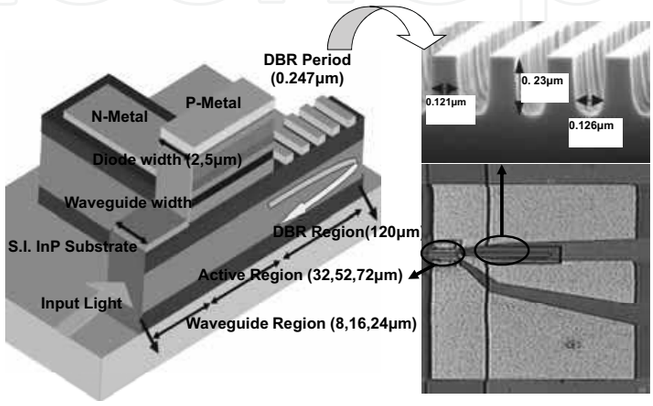

Fig. 3. The cross-sectional and top views of the demonstrated devices. The inset pictures the fabricated DBR mirrors.

The DBR mirror pairs (500 pairs), as labeled in Figure 3, are designed to produce a reflection maximum at around the 1550nm wavelength regime. The leaky optical waveguide used was composed of two lower undoped InGaAsP core layers, a thin heavily doped n-type InP etching stop layer, an $In_{0.53}Ga_{0.47}As$ based photo-absorption layer, 0.3μm undoped and 0.2μm p-doped in thickness, and a topmost p-type InP cladding

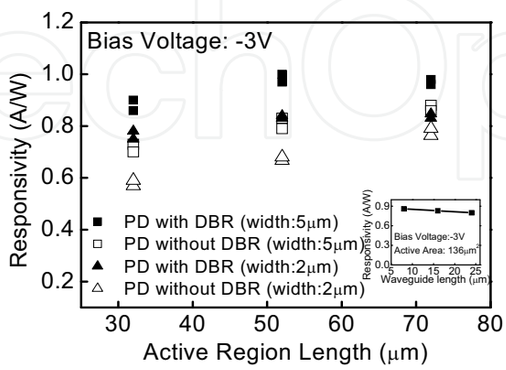

Fig. 4. The measured responsivity of both devices (with and without DBR mirrors) versus length of active diodes. The bias voltage is fixed at -3V and the waveguide widths of both

devices are 2μm and 5μm. The inset shows the measured responsivities of DBR devices with the same active area (136μm²) and different cleaved lengths of passive optical waveguide.

structure, without DBR mirrors, is around 200μm, and the theoretical calculated RC-limited bandwidth is just around 10GHz, in the case of a 50Ωload. By the incorporation of highly reflective DBR mirrors into our optical leaky waveguide, the required absorption-length can be shorten, meaning a superior bandwidth-responsivity performance product. The partially p-doped photo-absorption layer, shortens the thickness of the depletion layer and significantly increases the saturation current of the PD [10]. Figure 4 shows the measured maximum responsivity of both devices vs. the active diode lengths with different waveguide widths (2μm and 5μm). We can clearly see that all devices with DBR mirrors and different waveguide widths exhibit a much higher responsivity than that of the control device without DBR. The inset shows the measured responsivity of the DBR device vs. the cleaved waveguide length. We can clearly see that the measured responsivity is almost independent of the cleaved length. In comparison with the reported ECPD results, the measured responsivity will vary much more significantly (from ~0.7A/W to ~1A/W) when the cleaved length increases from 10μm to 20μm [7]. As shown in this figure, for a device with a DBR mirror, the achieved responsivity can be as high as 0.9A/W. Furthermore, our demonstrated device does not exhibit serious wavelength selectivity, which is a serious problem for the resonant-cavity-enhanced PD (RCEPD) [12]. This is because our cavity length is much longer than the operating wavelength and that an AR coating is applied to the input facet. The bandwidth and saturation current were measured with a heterodyne beating system. The traces shown in figure 5 (a) were from devices with and without DBR mirrors, with different active areas (96μm² and 136μm²) and almost similar responsivity performance (0.8 vs. 0.7A/W). Both devices were measured under the same dc bias voltage (-3V) and output photocurrent (5mA). Compared with the control, the device with DBR mirrors not only has higher electrical bandwidth performance (~40GHz vs. ~30GHz) but also produces higher bandwidth-responsivity (~32GHz-A/W vs. ~21GHz-A/W). Figure 5 (b) shows the measured frequency responses of devices with DBR mirrors and different active areas (96μm² and 160μm²) under a -3V bias voltage and a fixed 15mA output photocurrent. Even under such a high output photocurrent (15mA), both devices achieved

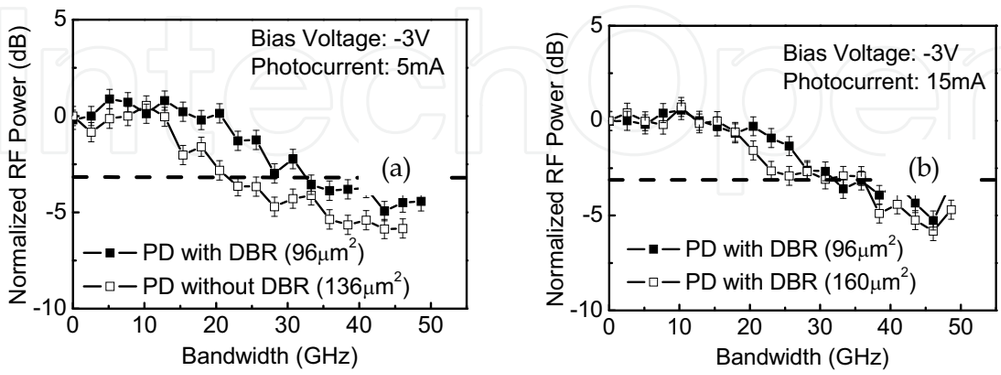

Fig. 5. (a) The measured frequency responses of devices under a fixed dc bias voltage (-3V) and output photocurrent (5mA). The active area of the devices, with and without DBR, is

96μm² and 136 μm², respectively. (b) The measured frequency responses of devices with DBR mirrors and two different active areas (96μm² and 160 μm²) under a fixed output photocurrent (15mA) and dc bias voltage (-3V).

an electrical bandwidth of around 40GHz. The high responsivity (0.8A/W and 0.9A/W) and high electrical bandwidth (~40GHz) that the demonstrated devices achieved under high current operation ensure their suitability for application to 40Gbit/sec analog and digital fiber communication systems. As compared to the results shown in Figure 5, we can clearly see that although the DBR device has larger active area than those of the control device (160μm² vs. 136μm²), the electrical bandwidth performance is still much better (~40GHz vs. ~30GHz) even under a much higher output photocurrent (15mA vs. 5mA). The superior high-power performance of the DBR device to the control device can possibly be attributed to its more uniform distribution of photo-generated carriers, because of the folded photo-absorption process. Figure 6 represents the photo-generated RF power versus dc photocurrent of devices under a fixed dc bias voltage (-3V). The ideal relation between the RF power of a 100% modulated large-signal and the average current with a 50Ω load is also plotted as a straight line for reference. As shown in this figure, DBR devices with a smaller geometric size (96μm² vs. 160μm²) can have a slightly larger photo-generated RF power under the same photocurrent, due to having a larger RC limited bandwidth. Furthermore, we can clearly see that the two DBR devices have a higher saturation current (~18mA vs. ~15mA) and RF power (6.4dBm vs. 2dBm) than that of the control devices with a 136μm² active area, due to their superior high power performance as discussed in Figure 3 and 4. The values achieved for RF power (6.4dBm), saturation photocurrent (~18mA), responsivity (0.8A/W), and electrical bandwidth (~40GHz) are comparable with the ECPD with PDP structure [16].

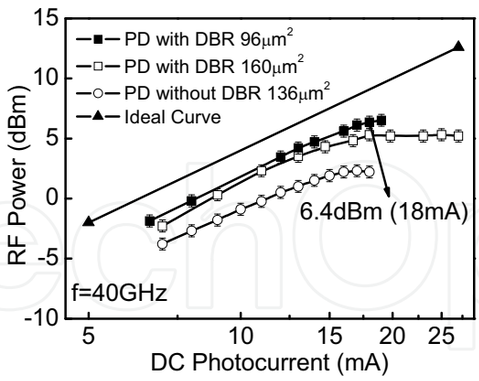

Fig. 6. The RF power versus dc photocurrent of both devices (with and without DBR) with three different active areas (squares: 96μm², open squares: 160μm², open circles: 136μm²) under a fixed 40GHz operating frequency and dc bias voltage (-3V).

2.3 Dual-Step Evanescently-Coupled Uni-Traveling-Carrier Photodiodes

A cross-sectional schematic diagram and the top view of the demonstrated DECPD are shown in Figures 7(a) and (b), respectively. Figure 7(c) shows a top view of the DECPD after zooming in on

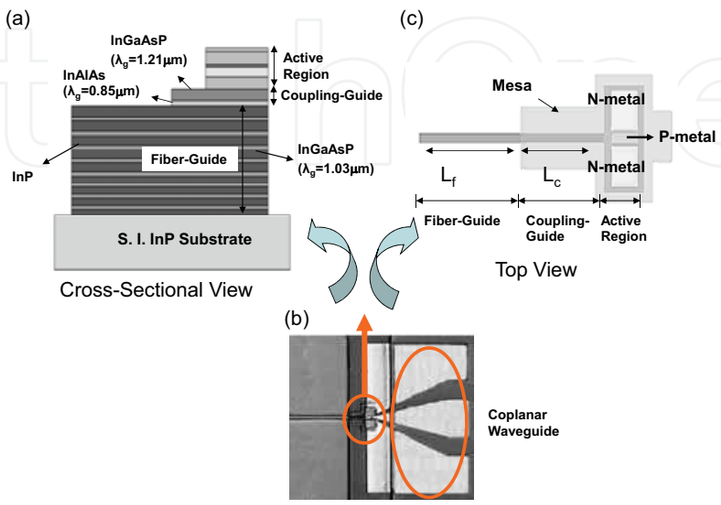

Fig. 7. (a) Cross-sectional view and (b) top-view of the demonstrated DECPD; (c) shows the top-view after zooming in on the active part of device. T and λ_g represents the thickness and bandgap wavelength of the specified epi-layer, respectively.

its active region. As shown in Figure 7(a), the first step in the bottom of our ECPD is a single-mode fiber-guide while the second step is the coupling-guide region. The lengths (L_f and L_c) of these two regions are marked in Figure 7(c). The fiber-guide is composed of nine InGaAsP layers, whose thicknesses increase from 100nm (bottom) to 314nm (top), in increments of 30nm, interspersed between the 80-nm-thick InP layers. In order to achieve low polarization dependence, low coupling loss, and maintain single-mode propagation, (which can benefit integration with other active or passive components in the planar-lightwave-circuit [17]), the index difference and thickness between InGaAsP and InP layers and the width (~5μm) and depth (~3μm) of the cross-section of our fiber-guide are all optimized using commercial three-dimensional (3-D) beam propagation method software (BPM). The insets to Figure 8 show the simulated mode spectrum and mode profile of light that propagates in the single-mode fiber-guide. Obviously, there is one significant dominant peak, of nearly 89% of the total input power, in this inset, which indicates that our fiber-guide can only support one mode (single-mode) propagation. We can thus understand that as the injected light couples into the upper coupling-guide region, it is always transferred with the same optical mode shape, regardless of the value of L_f, which is determined by the cleaving process. The second step in our passive waveguide is the coupling-guide region, which is composed of two n-doped InGaAsP ($1\times10^{18}cm^{-3}$) optical matching layers [8,9], for optical power coupling to the absorption region and good n-type ohmic contacts. The length of this coupling region L_c is precisely defined by the mask design rather than by the cleaving process. We can thus optimize L_c to achieve complete optical absorption for different active areas (lengths). Figure 8 shows the simulated optical

power distributions in our demonstrated devices. The simulated two DECPDs have the same active areas (76μm²) and active lengths (20μm), but different L_c (20μm and 35μm). The values of L_f obtained during the simulation are both around 300μm.

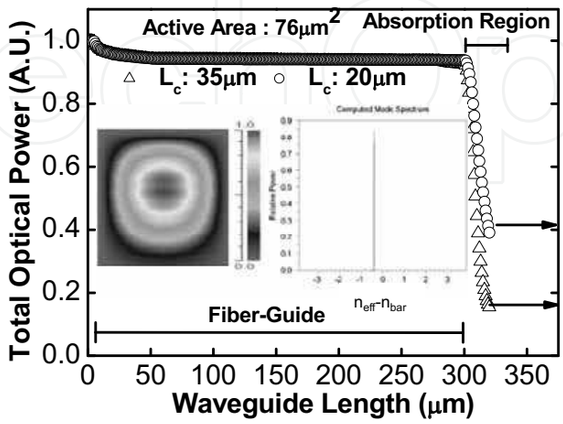

Fig. 8. Simulated optical power distributions without considering the optical scattering loss for devices with different coupling lengths and a fixed active area (76μm²). Triangle: L_c=35μm; circle: L_c=20μm. The arrowheads indicate the residual optical power after propagation through the active length (20μm). The insets show simulated cross-sectional views of the optical mode and mode spectrum in the fiber-guide region.

We can clearly see that by optimizing the value of L_c to be 35μm, the injected optical power for the active area (length) can be absorbed completely. The optimized values of L_c for devices with three different active areas; 56μm², 76μm², and 116μm², and a fixed waveguide width 2μm, are 40μm, 35μm, and 25μm, respectively. The active absorption region of our device has a typical UTC-PD structure [5]. The abrupt graded p-type doping profile ($2.5\times10^{17}\,cm^{-3}$ to $3\times10^{18}\,cm^{-3}$) in the absorption region is expected to minimize the speedy degradation phenomenon of our UTC-PD, especially when operating under a low output photocurrent [5]. Figure 9 shows the measured responsivity of our devices under a fixed bias voltage -3V and different polarization states versus different fiber-guide (cleaved) lengths L_f. The L_c of all the measured devices is fixed at 40μm. We can clearly see that the responsivity decreases as L_f increases, which may be attributed to the increase of optical scattering loss with L_f. The measured responsivity of our devices, which have the same 76μm² (56μm²) active area and different fiber-guide lengths (from 20μm to 50μm), is as high as around 1A/W (0.9A/W). The responsivity of the reported ECPD will oscillate seriously with the cleaved length (from ~0.7A/W to ~1A/W for cleaved lengths varying in the same range, 20μm to 50μm) [8,9]. We can thus conclude that, not only does our device demonstrate device high responsivity (~1A/W), but the cleaving tolerance is much higher (~around 50μm) than that of reported planar multi-mode ECPDs [8,9].

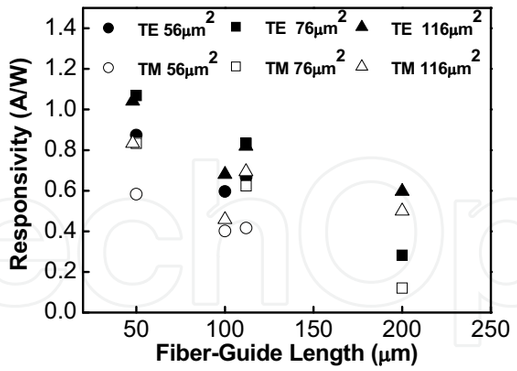

Fig. 9. Measured responsivity versus different L_f for devices with different active areas under a fixed bias voltage -3V.

The bandwidth and saturation current are measured with a heterodyne beating system. Figure 10 shows the measured frequency responses of the DECPD with different active areas under a fixed -1V bias voltage and a fixed photocurrent 5mA. The achieved 3-dB bandwidths of devices with actives areas of 56μm², 76μm², and 116μm² are around 60GHz, 50GHz, and 40GHz, respectively. The inset to Figure 10 shows the measured frequency responses of a device with an 116μm² active area under different reverse bias voltages and a small output photocurrent (0.5mA). We can clearly see that the speed performance of device is not degraded, even given such a small output photocurrent density (0.43kA/cm²) and different bias voltages. The past results reported for UTC-PDs indicate that they usually exhibit degradation of speed performance under low output photocurrent [5,18], which is an issue for high-speed fiber communication system [19]. The abrupt graded p-type doping profile in the absorption region of our device means that the static built-in electric field (1.6 to 19kV/cm) is around the critical field for the overshoot-velocity of the electrons. This in turn means that a smaller self-

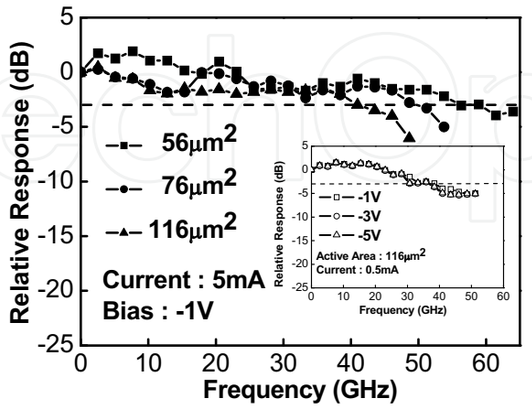

Fig. 10. Measured frequency responses of devices with different active areas under a fixed dc bias voltage (-1V) and a fixed output photocurrent (5mA). The inset shows the device

with an 116μm² active area measured under three different dc bias voltages (-1V, -3V, and -5V) and much lower output photocurrent (0.5mA)

induced field (photocurrent density) will be required to accelerate an electron to near its overshoot-velocity, thereby minimizing the problem of bandwidth degradation under low currents. Figure 11 shows the photo-generated RF power of the devices with (a) 56μm², and (b) 116μm² active areas. The three traces show the results measured under three different bias voltages (-1V, -2V, and -3V). The operating frequency is fixed at 60GHz and 40GHz for (a) and (b), respectively. The ideal relation between the RF power of a 100% modulated large-signal and the average current on a 50Ω load is also plotted as a straight line for reference. The maximum values of the RF power and dc photocurrent of the device with a 56μm² active area are limited by the thermal failure of the device. On the other hand, for a device with a larger active area (116μm²), significant saturation occurs at around 19mA photocurrent. The observed thermal-damage in our small device (56μm²) may be attributed to its larger electrical and thermal resistance, compared with that of a large device (116μm²). The values obtained for saturation current-bandwidth are around 780mA-GHz for both devices. In comparison with other reported high-performance ECPDs with a 25Ω effective load [20] or partially depleted absorbers (PDA)-ECPDs [16] with a 50Ω load, our demonstrated device can achieve a comparable bandwidth-responsivity (54GHz-A/W vs. 60GHz-A/W [20] and 40GHz-A/W [16]), and a higher saturation current-bandwidth performance (780mA-GHz vs. 520mA-GHz [20] and 680mA-GHz [16]).

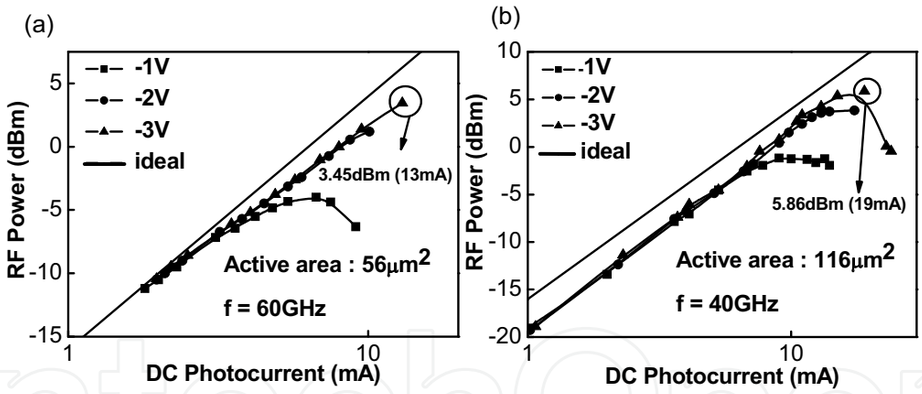

Fig. 11. The RF power versus dc photocurrent of both devices (with and without DBR) with three different active areas (squares: 96μm², open squares: 160μm², open circles: 136μm²) under a fixed 40GHz operating frequency and dc bias voltage (-3V).

3. Epitaxial Layer Structure of High-Power Photodiodes

3.1 Introduction

Ultra-high-speed and high-output-power performances are two main trends in the progress of all semiconductor-based devices for telecommunication. However, in most cases, speed and power performances are usually two-trade off parameters in the design of these devices, which include ultra-high speed PDs [4]. By properly down scaling the photo-

absorption volumes of PDs, ultra-high speed performances can be achieved, due to the reduction of parasitic capacitance and resistance in PDs. However, the small photo-absorption volume (~$1\mu m^3$) would cause a high density of photo-generated free carriers and induce a strong space charge field that screens the external applied bias field. The electrical bandwidth would thus seriously degrade due to the reduction in drift velocity of photo-generated carriers [4,5]. There are two major ways to increase the output saturation current (power) and electrical bandwidth product performances, the one is to distribute the photocurrents along edge-coupled PDs, such as the velocity matched distributed photodetector (VMDP) [12] and ECPD as we discussed before, the other is to shorten the carrier drift-time in the active photo-absorption volume, such as UTC-PD [4,5] and seperated-transport-recombintaion PD (STR-PD) [11]. In this chapter, we will introduce the fundamental trade-off between speed and power of ultra-high speed PDs, review the previous reported ultra-high speed/power PDs, and also our recent work about PD with state-of-the-art saturation current-bandwidth product performance.

3.2 Space-Charge-Screening (SCS) Effect in Photodidoe

Field-screening is a fundamental mechanism that limits the output power and electrical bandwidth of PDs under high optical power illumination. A simple model illustrates physical phenomena that mitigate field-screening effects in high-speed PDs, as discussed below. Filed screening arises when the dipole due to spatial separation of photo-generated charges, significantly reduces the drift field. This is especially serious when the photo-generated hole resides in the photo-absorption volume, due to its low mobility and the existence of hetero-structure barriers in p-i-n PDs as illustrated in Figure 12.

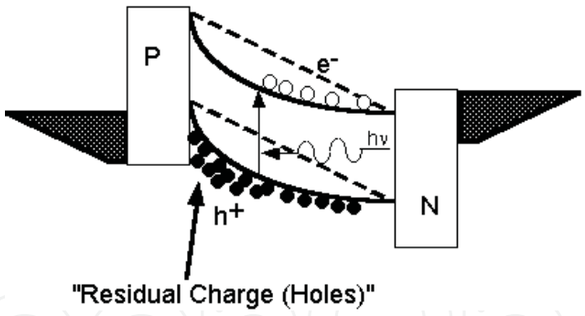

Fig. 12. The serious space-charge screening is originated from hole storage in photo-absorption volume.

The electric field in the photo-absorption layer is the sum of the built-in field (E_b), the field due to photo-generated free charges (E_f), and the fields of waves originating elsewhere and propagating inside the structure (E_w), $E = E_b + E_f + E_w$. The space charge field is found by Gauss's law and is proportional to the charge area density. For simplicity and clarity, the built-in field and the charge densities of the electrons and holes are approximated as rectangle functions in Figure 13. Figure 13 shows three sets of conceptual graphs at successive times after photo-generation of electrons and holes in the photo-absorption volume by a short optical pulse. The upper plot shows the photo-generated charge densities,

and the lower plots show the net electric field in the absorption region. Electron and hole velocities are assumed equal. The field resulting from the separation of the free charges opposes the built-in field, and if the charge density is large enough, may actually cancel it, as shown in the third set of graphs. Further, besides these, from the above figures, we can clearly see that the region with the least electric field is near the center of absorption region, where the carriers, especially for the case of hole, in the low-field region will travel slow, causing a slow component in the device photocurrent response. Field-screening is said to occur when the device response is perceptibly affected.

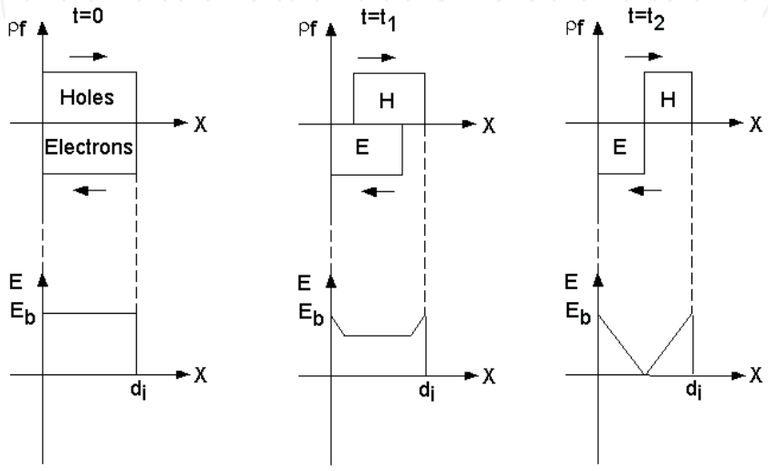

Fig. 13. Conceptual illustration of field-screening mechanism. Simplified electron and hole distributions and net electric fields in the depletion region are plotted at three times after photo-generation by a short optical pulse.

$$E_{eff} = \left(\frac{V_{bais} - Z_{load} \times J \times A + V_{bi}}{D} \right) - \left(\frac{J \times D}{V_{hole} \times \varepsilon} \right) \quad (1)$$

$$V_{hole} = V_{pl} \times \tanh\left(\frac{\mu_h \times E_{eff}}{V_{pl}} \right) \quad (2)$$

Symbol	Quantity & Value
E_{eff}	Effective electric field intensity (V/m)
V_{bais}	Applied voltage (V)
A	Active area of photodiode
J	Generated current density (A/m^2)
V_{bi}	Built-in voltage of diode (0.7 V)
D	Depletion layer thickness(m)
ε	Dielectric Constant of InGaAs ($1.23*10^{-10}$ F/m)
V_{hole}	Hole Velocity (m/s)
V_{pl}	Maximum Hole Velocity ($4.8*10^4$ m/s)
μ_h	Hole Mobility ($60\ cm^2/Vs$)
Z_{load}	Load Impedance ($50\ \Omega$)

Table 1. Symbols and quantities for equation (1) & (2)

Eq. 1 and 2 is the transcendental equation for solving the net magnitude of electric field in the photo-absorption region and the drift velocity of photo-generated hole, respectively. The

physical meanings and values of each parameter are given in Table 1. We can clealrly see that in order to increae the E_{eff} and saturation current of photodode, we must reduce the depeletion layer thickness (D) or increase the carrier drift-velocity (V_{hole}). By increasing the drift-velocity of photo-generated carriers, such as with the structure of a UTC-PD, is one way to minimize the SCS effect. Excellent high-speed and high-power performance has been demonstrated [4,5] in UTC-PD. Figure 14 shows the conceptual band diagram of UTC-PD. Compared with the traditional p-i-n structure, the photo-absorption layer in the UTC-PD is a p-type doped epi layer instead of an intrinsic layer, thus the photo-generated holes will relax to the p contact metal directly without drift, diffusion or accumulation in photo-absorption layer, which will cause serious bandwidth degradation due to the space-charge screening effect. The photo-generated electrons in the absorption layer will diffuse into an intrinsic layer. In order to reduce the diffusion time of electrons in p-type layer, graded-doped or graded-bandgap absorption layers have been demonstrated in UTC-PDs [4,5] as in the n-p-n hetero-junction bipolar transistor (HBT) devices. Without the poor transport properties, such as low mobility and low drift velocity of the photo-generated holes, high power-bandwidth product performance of VPD type, WGPD type, and distributed type UTC-PDs have been demonstrated [4,5,21].

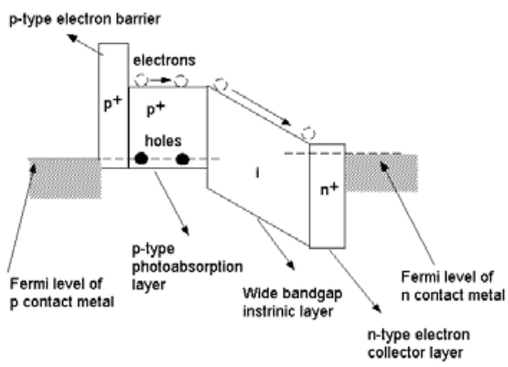

Fig. 14. The conceptual band diagram of UTC-PD

3.3 Near-Ballistic Uni-Traveling Carrier Photodidoe (NBUTC-PD)

The structure of UTC-PD, as discussed before, has attracted much attention due to its excellent speed and output power performance. However, such a device usually suffers from the problem of bandwidth degradation under high dc external bias voltage [4,5] due to both the high electric field existing at the junction of the collector (C) and photo-absorption (P) layer, and the decrease in the overshoot drift-velocity of photo-generated electrons. One possible way to enhance the speed performance of UTC-PD is to reduce the externally applied bias voltage and let the value of the electric field in the C-P junction approximately for the critical field, which will enhance the drift-velocity of photo-generated electrons [4,5]. However, under such low reverse bias voltage (around -1V for 200nm collector), the field-screening effect, which originates from the difference in polarity between the output ac voltage across the standard 50Ω load and the dc bias voltage, will seriously limit the maximum output photocurrent of the UTC-PD. Near-ballistic UTC-PD (NBUTC-PD) with state-of-the-art performance has been demonstarted to overcome the above-mentioned problems [22,23]. By inserting an additional delta-doped p^+ charge layer and an electric-

field-suffer layer into the collector layer, we can produce an appropriate value of electric field in most of the collector layers so as to sustain a peak velocity of photo-generated electrons under certain ranges of bias voltage and output photocurrent.
Figure 15 shows the conceptual band diagram of InP based NBUTC-PD. The major difference in the epi-layer structure between the UTC-PD and the demonstrated NBUTC-PD is the additional planar-doped p^+ $In_{0.52}Al_{0.48}As$ charge layer and the 100nm thick undoped $In_{0.52}Al_{0.48}As$ electric-field-suffered layer (E). The basic working principle of the NBUTC-PD is similar to that of the reported "Ballistic Collection Transistor (BCT)" [24], whose near-ballistic transport property has been verified through Monte Carlo simulations and experiments [25]. By introducing the proper planar doping density ($5\times10^{11}cm^{-2}$) into the depleted p^+ charge layer, the maximum electric field in the $In_{0.52}Al_{0.15}Ga_{0.33}As$ collector layer can be controlled to produce an appropriate value (around 40kV/cm at -5V bias) to sustain the overshoot velocity of the photo-generated electrons under a certain range of bias

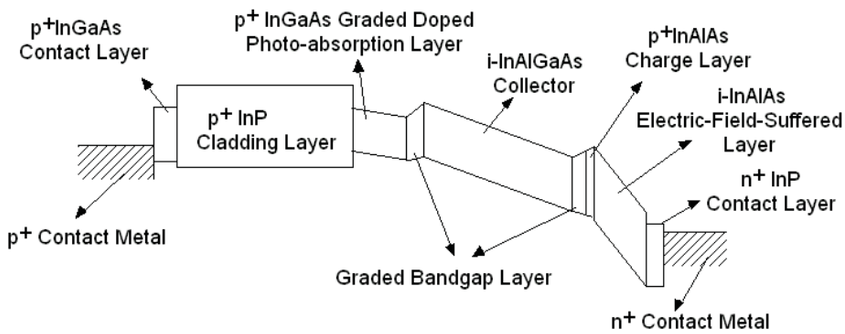

Fig. 15. The conceptual band diagram of NBUTC-PD

voltages and output photocurrents. The adopted graded p-type doping profile of the P layer can produce a built-in electric field (1.6 to 19kV/cm) around the critical field for the electron overshoot velocity. This means that a small self-induced field (photocurrent density) will be required to accelerate an electron to near its overshoot-velocity in the P layer [15]. Through this special P and C two-layer design, near-ballistic-transport of photo-generated electrons throughout the whole epi-layer structure can thus be expected. NBUTC-PDs with ECPD and back-side illuminated VPD structures [22,23] have both been demonstarted. Both kinds of strcuture have demonsatrted ecellent speed and power performance.
Figure 16 (a), (b) shows cross-sectional view and top views of the demonstrated NBTUC-PD with ECPD structure, respectively. The optical waveguide structure of our demonstrated NBUTC-PD is based on the reported high-performance planar evanescently-coupled photodiode as discussed before [8,9]. Extremely high responsivity of 1.01A/W and 1.02A/W was achieved with 150μm² and 200μm² active areas, respectively. The responsivity of the device with an 8μm waveguide/diode width and 40μm (320μm² active area) absorption length could be further improved to 1.14A/W. To our knowledge, these are the highest values ever reported for the responsivity of high-speed and high power UTC-PDs [4,5]. Figure 17 shows the typical frequency responses of the device with a 200μm² active area under different levels of the output photocurrent (0.5mA, 5mA, and 20mA) and a fixed dc bias voltages (-5V). One can clearly see that under 0.5 and 5mA operation, the electrical

bandwidth was around 40GHz. When the photocurrent reached 20mA, the bandwidth of device increased to 50GHz. Figure 18 shows the measured and fitted frequency responses of the device with a 320μm² active area under 10mA and 15mA

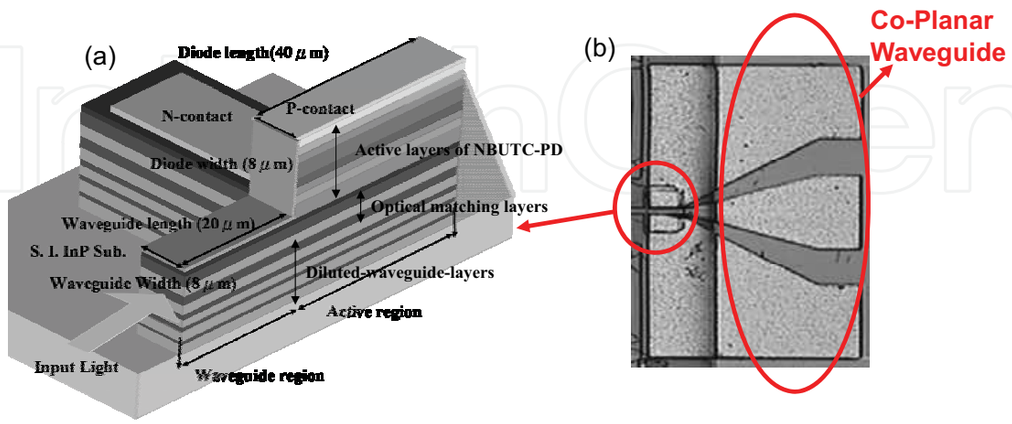

Fig. 16. Cross-sectional view (a) and top-view (b) of NBUTC-PD, which incorporates with an evanescently-coupled optical waveguide.

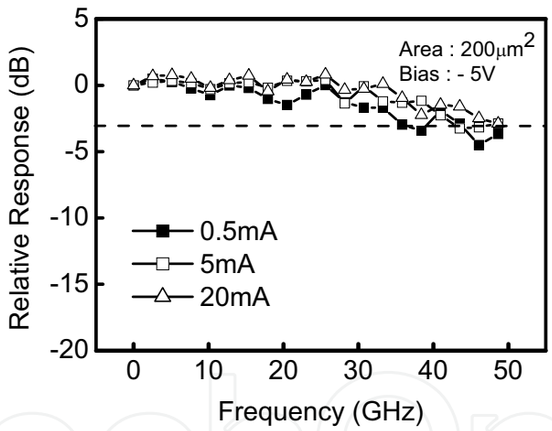

Fig. 17. The measured frequency responses of the device with a 200μm² active area under different levels of the output photocurrent and a fixed dc bias voltage (-5V). (square: 0.5mA; open square: 5mA; open triangular: 20mA).

output photocurrent values. The dc bias voltage was fixed at -4V. According to our simulation results, the bandwidth improvement under high current operation (15mA) is associated to the reduction of the transport time as discussed above and the ac capacitance [18]. The total capacitance is reduced due to the subtraction of the differential ac capacitance $I_C \times (d\tau_C / dV_{ac})$, proportional to the current, from the depletion capacitance [13,18]. Where, V_{ac} is the output ac voltage of device, I_C is the photocurrent, and τ_C is the

electron drift time. For the case of demonstrated device, such effect should be significant due to that under near-ballistic transport, the variation of drift-velocity (time) vs. the electric field (V_{ac}) is obvious, according to the reported field dependence electron drift velocity of III-V semiconductors. On the other hand, for the case of UTC-PD operated in the velocity-saturation regime, such effect can almost be neglected due to the fact that electron velocity is insensitive to the electric field. In our bandwidth simulation model, we thus used different

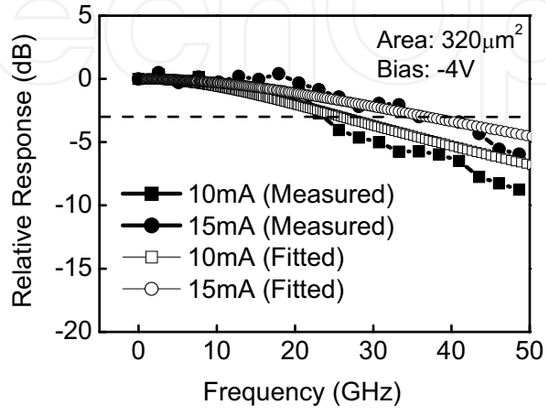

Fig. 18. The measured and fitted frequency responses of the device with a 320μm² active area under different output photocurrent values and a fixed dc bias voltage (-4V) (square: measured trace under 10mA operation; circle: measured trace under 15mA operation; open square: fitted trace under 10mA operation; open circle: fitted trace under 15mA operation.).

drift-velocities and the variation of slopes of electron drift-velocity vs. the electric field in $In_{0.53}Ga_{0.47}As$ material to roughly estimate the reduction of total capacitance and fit the measured frequency responses. Figure 19 shows the fitted and measured microwave S_{22} parameters of NBUTC-PD with a 320μm² active region for a broad frequency range (from 40 MHz to 50 GHz) under two different output photocurrents (1mA and 20mA) and a fixed bias voltage of -5V. The obvious difference between the S_{22} parameters under low and high photocurrents indicates the variation of the elements' values in the equivalent-circuit-model. Under high current operation (20mA), the traces of S_{22} in the Smith-Chart are closer to the S_{22} traces of the case of ideal open-circuit than the measured S_{22} trace under low current operation (1mA) are, which implies a significant improvement in the microwave characteristics of device. This phenomenon has never been observed before in the traditional p-i-n PD. The measured frequency responses of the S_{22} parameters of ordinary PDs or UTC-PD are usually insensitive to their output photocurrent [26]. As compared with the reported UTC-PD [4,5], NBUTC-PD can achieve almost the same electrical bandwidth (around 40GHz), even with a much larger device size (320μm² vs. ~120 μm²), and responsivity. This implies that the NBUTC-PD can achieve better output power and responsivity performance with a larger device size without sacrificing speed seriously due to the superior transport property of photo-generated electrons. The traces shown in Figure20 represent the photo-generated RF power vs. dc photocurrent of the NBUTC-PD under different bias voltages (-1V, -3V, and -5V).

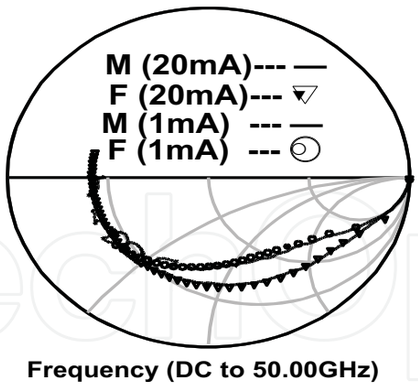

Fig. 19. The measured and the fitted S_{22} parameters of the device with a 320μm² active area under different levels of output photocurrent (1mA and 20mA) and a fixed dc bias voltage (-5V). The two solid lines represent the measured S_{22} under 1mA and 20mA. Traces with open circle and close triangle symbols represent the fitted results under 1mA and 20mA, respectively.

The operating frequency was fixed at 40GHz. The ideal relation between the RF power of a 100% modulated large-signal and the average current on a 50Ω load is also plotted as a straight line for reference. For the case of a –5V bias, the traces of the device with different active areas (200μm² and 320μm²) are also shown for the purpose of comparison. Since, the bandwidth of the device with a 320μm² active area increases as the photocurrent increases significantly under a -5V bias, the output RF power is closer to the ideal line than is the case with a low photocurrent.

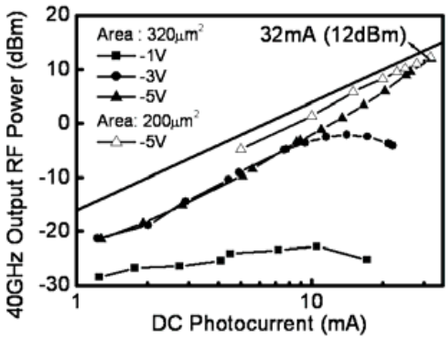

Fig. 20. RF power versus dc photocurrent of the devices with different active areas under different reverse bias voltages (square: -1V, circle: -3V, triangle (open triangle): -5V) at a 40GHz operating frequency. The ideal relation between the RF power and current on a 50Ω load is plotted as a straight line for reference purpose.

As compared to the structure of ECPD, the VPD structure may have further improved high-power performance due to that the input-end saturation problem can be eliminated. However, its responsivity may be poorer. Fortunately, when the operation frequency is over 100GHz, the maximum output saturation power from PD becomes a key isssue instead of efficiency due to that the over 100GHz MMW power amplifier still remains a challenge. The

key point to pursuit the ultimate high saturation current-bandwidth product of the PD is to downscale the area of the photo-absorption active area and the thickness of the depletion layer. However, device-heating [6] and high parasitic resistance could become problems, which would seriously limit the saturation current of a PD with such a small active area (~10μm²). It has been demonstrated that such problems can be minimized by the incorporation of flip-chip bonding structures or an epitaxial layer transferring process [27]. Figures 21 (a) to (d) show the top view of the NBUTC-PD with VPD structure before flip-chip bonding, cross-sectional views of the device, the flip-chip bonded NBUTC-PD, and the layout of the flip-chip bonding pedestal, respectively. The details of the geometric structure of the back-side illuminated NBUTC-PD are similar to those described in our previous work [25]. Figure 22 (a) and (b) shows the measured O-E frequency resposne and measured output photocurrent vs. MMW power of NBUTC-PD with a 144μm² active area, respectively. The measured saturation-current bandwidth product is a record-high, over 4070mA-GHz (>110GHz, 37mA). This is superior to all values reported for high-performance evanescently-coupled p-i-n PDs (624mA-GHz, 120GHz, 5.2mA) [20], parallel-fed traveling wave photodetectors (1760mA-GHz, 80GHz, 22mA), [17], and UTC-PDs (>2380mA-GHz [4], (2500mA-GHz [28])) under the similar heterodyne-beating CW-measurement.

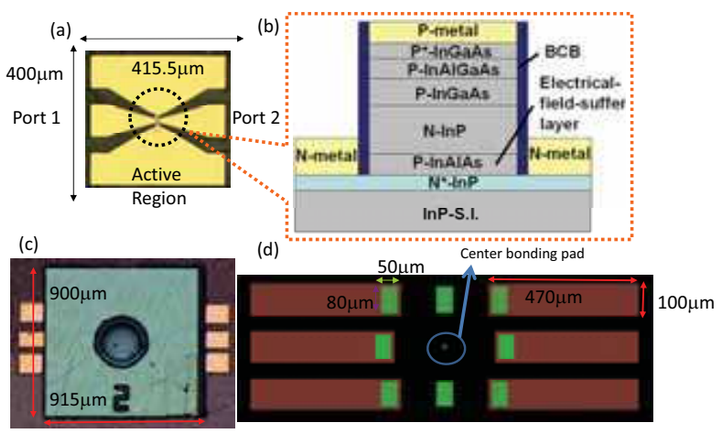

Fig. 21. (a) Top-view of the NBUTC-PD, (b) conceptual cross-sectional view of the NBUTC-PD (c) NBUTC-PD after flip-chip bonding, (d) and flip-chip bonding pedestal.

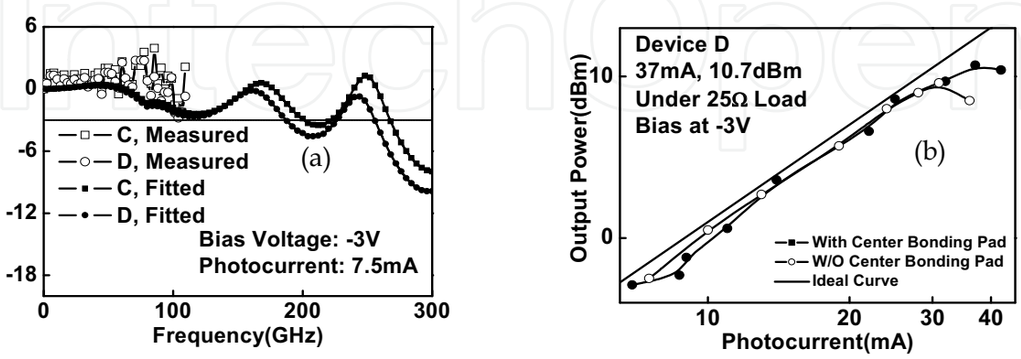

Fig. 22. (a) The measured and fitted O-E frequnecy resposne of NBUTC-PD with VPD structure. Device C and D have 100μm² and 144μm² active areas, respectively.

3.4 Partially-Depleted PDs

Thinng the absorption layer thickness [4] or using the p-type absorption layer [4,5], such as the case of UTC-PD, are both possible ways to increase the saturation power of PD, however, the quantum efficiency performance of PDs are usually sacrificed due to its thin intrinsic layer or the recombination process of photo-generated carriers in the photo-absorption layer with p-type dopant [1,11]. Recently, some research groups have demonstrated a new photodiode design that combines the depleted and neutral absorption layers (p-type doping) to maximize the bandwidth-efficiency product of photodiode [10]. Excellent bandwidth

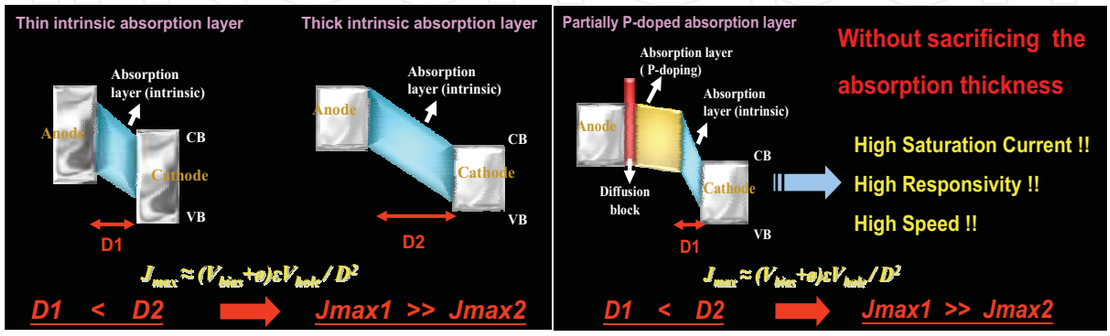

Fig. 23. The conceptual picture, which illustrate why that the PDP structure can have higher stauration current than that of a traditional p-i-n diode.

(over 50GHz) and efficiency performance (0.98A/W) have been demonstrated by use of such technique with the structure of vertical-illuminated PD. Figure 23 shows the conceptual band diagram of a partially depleted PD (PDP) and a traditional PD with a pure intrinsic absoprtion layer. We can clealy see that by replacing some part of intrincsic absoprtion layer with p-type doping layer, the depeltion layer thickness can be downscaled and the drift-time of photo-genearted hole can be effectively reduced. The diffsuion time of electron in the p-type absorption layer is not an isse due to that it can be minimized by use of the graded doping profile to create a built-in electric field and accelearte the diffusion process. Such technique has already been reported in the UTC-PD structure [4,5]. Futhermore, the PDP structure can have superior responsivity performance to the high-power PD by downscaling the absorption layer thickness. ECPD with PDP structure as active photodidoe [9] have already been demonstarted. In order to study the influence of

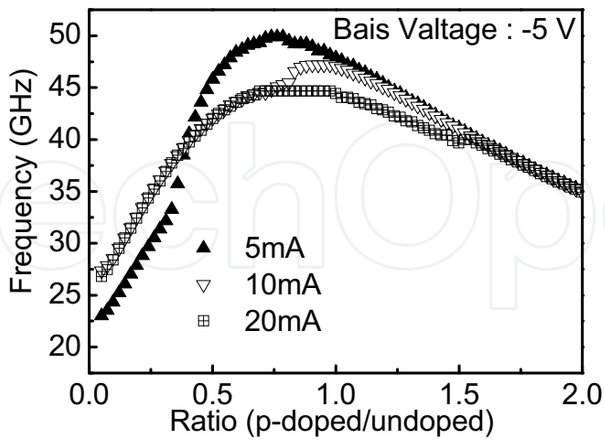

Fig. 24. The simulated electrical bandwidth vs. the ratio of p-doped photo-absorption layer thickness to undoped photo-absorption layer thickness under different operation current (5, 10, 20 mA). The thickness of InGaAs photo-absorption layer is fixed at 500nm.

partially p-doped photo-absorption layers on the high power performance of photodiode, two kinds of devices, which have the same structures of epi-layers except for the photo-absorption active region, were fabricated. Device A has the graded partially p-doped photo-absorption layer to accelerate the drift velocity of photo-generated electrons and device B has a pure intrinsic photo-absorption layer. The ratio of p-doped to undoped layer thickness of device A has been optimized due to the trade-off between RC time constant and drift time of photo-generated carriers [29]. Figure 24 shows the simulation result. As can be seen, by choosing that the ratio of p-type layer thickness over the total absorption layer thickness, which is fixed at 0.5μm, equals to 0.5, we can get a optimized speed performance. The measured DC responsivity of both devices are the same as 1A/W. The measured frequency responses and f_{3dB} electrical bandwidths of device A and B are shown in Fig. 25 (a). Device A and B have the same sizes of active area (150μm^2) under the same dc bias voltage (-1V) and output photocurrent (5.5mA). According to the measurement results, we can clearly see that device A with partially p-doped photo-absorption layer has superior electrical bandwidth

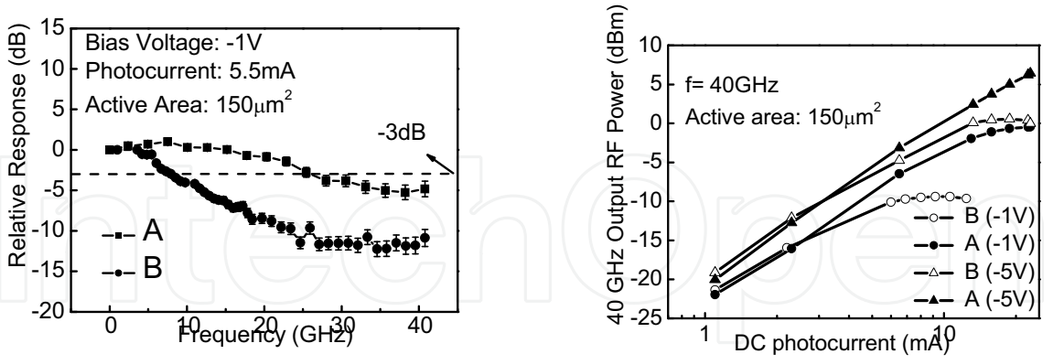

Fig. 25. (a) The measured frequency responses of device A and B under the same high output current (5.5mA) and dc bias voltage (-1V). The active area of device A and B is about 150μm² (b) RF power versus dc photocurrent of device A and device B under different reverse bias voltages (close triangle: -5V of device A, open triangle: -5V of device B, close circle: -1V of device A, open circle: -1V of device B) at 40GHz operating frequency. The active area of both devices is 150μm².

performance (~26GHz vs. ~8GHz) especially under high current (5.5mA) and low bias voltage operation (-1V). Fig. 25 (b) shows the photo-generated RF power versus dc photocurrent of device A and B with the same active area (150 μm²) under different reverse bias voltages (-1V and -5V). As this figure indicates, both devices exhibit significant saturation behaviors under low bias voltage (-1V) and high current operation (~10mA). Besides, device A has significant higher values of RF saturation power then device B especially under low dc bias voltage (-1V). These measurement results, as shown in Fig. 23 to 25, indicate that the technique of partially p-doped photo-absorption layer will enhance the speed and output power performance of photodiode significantly without sacrificing the responsivity performance. Furthermore, as compared to downscale the thickness of intrinsic InGaAs photo-absorption layer directly, this demonstrated technique would not increase the device absorption length or sacrifice the responsivity.

3.5 Separated-Transport-Recombination PDs

Based on equation 1, downscaling the depletion layer thickness is the most straightforward way to increase the saturation power of a photodiode [4,11] due to the shortening of carrier drift-time. However, PDs with thin depletion layers usually suffer from the problems of low quantum efficiency and very limited RC bandwidth. As discussed before, PDP structure is one kind of structure to overcome the above-mentioned problems, however, its speed performance may still be limited by the drift-diffusion time of carriers. A novel p-i-n photodiode structure: the Separated-Transport-Recombination photodiode (STR-PD), which can greatly relieve the trade-offs among output saturation power, quantum efficiency, and electrical bandwidth performance, have been demonstarted to further imprve the speed performance [11]. In the demonstrated GaAs based STR-PD, the LTG-GaAs layer, which has an extremely short carrier lifetime (less than 1ps) [30], is adopted to serve as the recombination center in the active photo-absorption region and futher break the bandwdith

limitation of drift-diffusion time of photo-genearted carreiers. Figure 26 shows a conceptual band diagram of the STR-PD. The LTG-GaAs layer with an extremely short

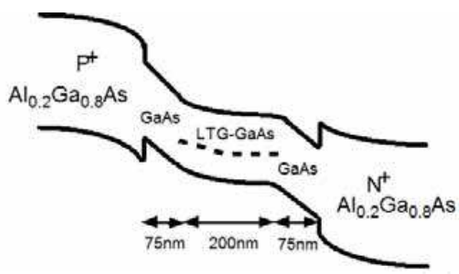

Fig. 26. The conceptual band diagram of the demonstrated STR-PD.

carrier lifetime [30] serves as a recombination center sandwiched between two high quality GaAs based photo-absorption layers. As shown in Fig. 26, the external applied electric field is concentrated in the two GaAs layers due to the high defect density and field-screening effect of the inserted LTG-GaAs layer [11]. These two photo-absorption layers can, thus, be treated as a "transport layer" or "depletion layer" in our structure due to their much higher mobility compared to LTG-GaAs and the concentration of the applied electric field. To recombine the photo-generated carriers, which exhibit low drift-velocity under high current operation, the position of this inserted LTG-GaAs based layer is located near the center of the photo-absorption region [4]. Under optical illumination, most of the photo-generated electrons in the transport layer, which is near the P^+ $Al_{0.2}Ga_{0.8}As$ layer, will be injected into the LTG-GaAs layer and will recombine with the photo-generated hole from the other side of transport layer. The effective carrier-drift distance in the STR-PD will be roughly approximated by the thickness of the one-sided GaAs based photo-absorption (depletion) layer, which can be thinned down to shorten the drift-time of photo-generated carriers and increase the output saturation current. In our structure, the trade-off between the output saturation current and R-C bandwidth limitation can also be relieved significantly due to the increase in the thickness of the total intrinsic (i) layer, which is composed of undoped GaAs and LTG-GaAs layers with high resistivity, and to the reduction of the device capacitance without affecting the carrier drift-time. Compared with the traditional p-i-n photodiode, it can minimize the RC bandwidth limitation by increasing the thickness of the intrinsic photo-absorption layer directly. However, the drift-time will be increased and the output saturation power will be seriously degraded [4]. Due to the separation of the transport layer (GaAs) from the recombination layer (LTG-GaAs) in our STR-PD structure, the applied electric field will be concentrated in the two GaAs based transport layers, and the problems of low drift-velocity and lifetime increasing effect of the LTG-GaAs based layer can, thus, be compromised [31,32]. In order to study the influence of the recombination layers on the high power performance of photodiodes, two kinds of devices, which have the same epi-layer structure except for the photo-absorption active region, were fabricated. As shown in Fig. 26, device A has an LTG-GaAs-based recombination layer with a 200nm thickness in the center of the photo-absorption region, and the thickness of the surrounding GaAs layer is 75nm. Device B has a pure GaAs based photo-absorption layer with a 350nm thickness, which is around five times thicker than the effective carrier-drift distance of device A (350nm vs. 75nm). The two types of fabricated devices have the same geometry of the WGPD, which can achieve bandwidth-efficiency product performance superior to that of

VPDs as discussed before. A mode-locked Ti:sapphire laser, which has a center wavelength of 850nm, as the light source for dc photocurrent and ac transient measurements. Figure 27 (a) and (b) shows the FWHM of the measured impulse responses versus reverse bias voltage, respectively. As the diagrams indicate, device A achieved better speed performance than device B especially under a high output photocurrent and low dc bias voltage. Furthermore, we can clearly see that in the case of device A, the measured FWHM was insensitive to both the reverse bias voltages (-1 ~ -7V) and input optical power (0.02mW, 0.4mW). As shown in Fig. 27(b), the lifetime increasing effect of the traditional LTG-GaAs based p-i-n photodiode under a high dc bias voltage [30] is eliminated in our novel structure due to the concentration of the applied electric field in the GaAs based transport layers.

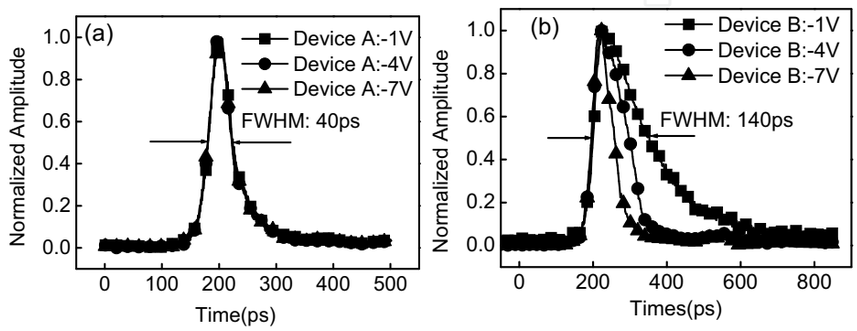

Fig. 27. The normalized impulse responses of device A (a) and device B (b) with a 400μm^2 active area under a fixed optical pumping power (0.4mW) and different reverse bias voltages (-1V, -4V, -7V).

4. The Application of High-Power PDs to ROF Communication System

4.1 High-Power PD for RoF Communication and Nonliner Photodetection Scheme

As discussed in the introduction, the "killer application" of high power PD is in the RoF communication system. In this system, high-power PD is used for converting the intense optical power to strong MMW signal and then radiating it to the user-end in last-mile. Photonic transmitter [2, 33-35] (PT), which is composed of a high-power PD and printed-circuit antenna, has thus been demonstrated to match such application. Futhermore, the nonlinear photodetection scheme [36,37] of high-power PD is usually adopted in RoF system to eliminate the necessity of MMW electronic mixer and remote signal re-generation [38]. In this section, we will review several kinds of photonic transmitter and introduce the nonlinear operation of NBUTC-PD based PT for the application of W-band RoF system.

4.2 Photonic Transmistter

Figure 28 (a) and (b) shows a top view of the demonstrated PTs through the use of flip-chip bonding (hybrid) and monolithic integration of PDs with antenna, respectively.

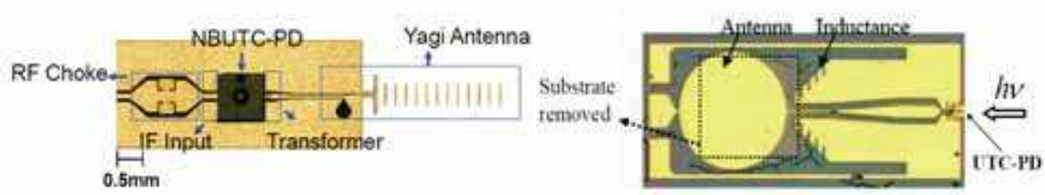

Fig. 28. (a) Top-view of the flip-chip bonding and (b) monolithic integrated photonic transmitters.

In Fig. 28 (a), the integrated active PD is NBUTC-PD, and the passive antenna is quasi-Yagi antenna with end-fire pattern [35]. The active NBUTC-PD is flip-chip bonded with antenna on an AlN substarte. As compared to the reported UTC-PD based PT with taper-slot antenna (TSA) also with end-fire pattern, the size of our quasi-Yagi antenna [39] has comparable directivity (~10dB) and is more compact than that of TSA. In addition, the quasi-yagi antenna is more immune to the substarte–modes, which should be a serious issue of antenna when the operating frequency is over 100GHz, than those of other kinds of planar antenna, such as dipole, slot, and TSA [40]. In Figure 31, the integarted active PD is STR-PD and the antenna is circular disk monopole antenna with broadside pattern [41]. By use of such PT under 850nm femto-second Ti:sapphire mode-locked laser excitation, high radiated peak power without using Si substarte-lens can be achieved [34]. As discussed before, NBUTC-PD has strong bias dependent speed performance. By use of such characteristics, high-power and low up-conversion-loss optoelectronic mixer, which is used for nonlinear photodetection system [36], has been demonstrated [35,42]. Compared with UTC-PD based OE mixer, NBUTC-PD based OE mixer can have wide operation (up-conversion) bandwidth due to the forward bias operation is eliminated [43]. Figure 29 shows the system setup of BPSK and QPSK RoF wireless data tranamission system. In such system, the NBUTC-PD based PT, as shown in Figure 28(a), is adopted to convert the optical LO signal at 100GHz to electrical and the electrical QPSK and BPSK data signal is injected onto the NBUTC-PD and the bias point of device is thus modulated by injected signal. The QPSK or BPSK data signal is then up-converted to W-band and radiated to the receiver end. Compared to the traditional On-Off Keying (OOK) data transmission process [1] using a PT, the modulation format of the BPSK and QPSK techniques allows for higher spectral efficiency and is compatible with today's wireless communication systems. In order to realize the goal of free-space data transmission, a high-performance W-band optical photonic source [44] is installed in such system. The inset to Figure 29 shows the output optical spectrum from this optical source. As can be seen, the optical harmonic distortion suppression ratio is 18 dB, and is limited by the bandwidth of our dual-parallel E-O modulator (i.e., 10 GHz) [44]. This source is much less noisy than the two-laser heterodyne-beating system, which was used for device characterization. During the experiment, the BPSK signal is a 1.25Gbit/sec pseudo random bit sequence (PRBS) 2^{31}-1 signal. The 0.625Gbit/sec QPSK signal is generated by an arbitrary waveform generator (AWG) at a data rate of 625Mb/s. The receiver end is composed of a W-band horn antenna, a W-band low-noise-amplifier (LNA), and a fast W-band power detector to detect the envelope and phase of data signal. The signal detected by the power detector is boosted by an IF amplifier

and then fed into a high-speed real time scope prior to performing off-line signal processing.

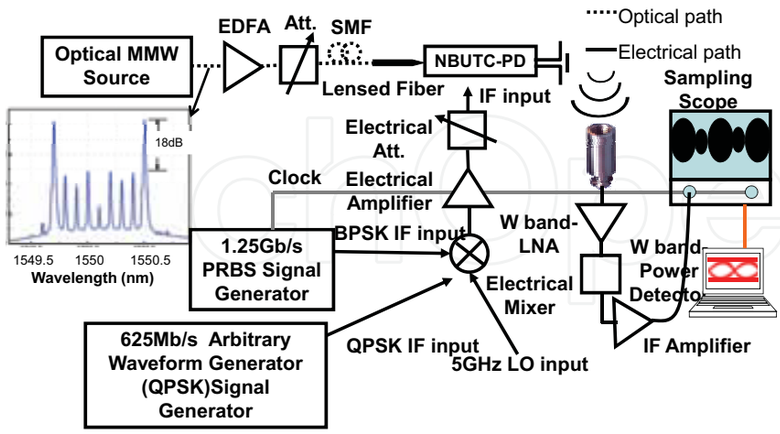

Fig. 29. The system setup for BPSK or QPSK data transmission.

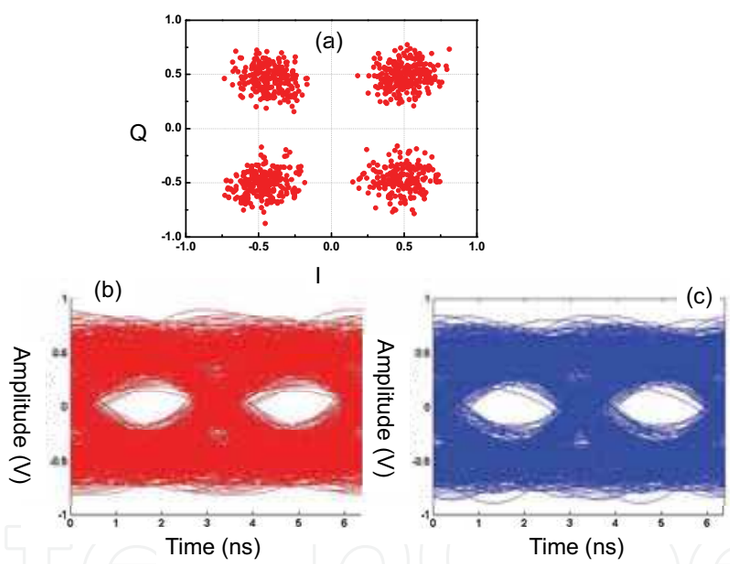

Fig. 30. (a) Constellation of the 0.625-Gb/sec QPSK signal. Eye diagrams of the 0.625-Gb/s QPSK signal: (b) I; (c) Q.

Figure 30 (a) shows the constellation of the received 0.625-Gb/s QPSK signal when the output photocurrent is 10mA; while (b) and (c) show the digital signal processing (DSP) re-constructed I and Q eye diagrams. The corresponding EVM is around 24.7%.

5. Conclusion

The motivation for developing high-power and high-speed PDs arises from the power and speed limitations on conventional p-i-n PDs. There are two approaches to improve the high-power performance of PDs without downscaling the device active area aggressively and seriously sacrificing its responsivity. One is to distribute and uniform the photocurrents along the edge-coupled PDs by improving the geometric structure of optical and electrical waveguides, such as, evanescently-coupled photodiode (ECPD); the other is to minimize the space-charge effect in the photo-absorption volume by changing the structure or material of epitaxial layers, such as UTC-PD, PDP, and STR-PD.

In this book chapter, at first, we discusssed the geometric structures of high-power PD. In order to overcome the significant variation of quantum efficinecy vs. cleaved length in the traditional ECPD, two kinds of strcutrure have been discussed. One is DECPD and the other is the leaky-waveguide with DBR mirror. In the structure of DECPD, the fiber-coupling waveguide and absorpion-layer coupling wavegudie is seperated in space and the celaved tolearnce can thus be grealty improved. With repsect to the structure of leaky-waveguide PD with DBR mirror, it can reduce the required photo-absorption voulme due to the optical path is folded and the improvement in O-E bandwidth. Excellent high-responsivity and high-saturation-current-bandwidth product perfroamnce have been demonstarted by use of both structures.

In the second part of this chapter, we discuss the mechansim of saturation of PD under high-power operation and disclsoe several kinds of high-power PDs to overcome the limiation of high-power performance. The key issue to improve the high-power performance of PD is to shorten the carreir drift time inside the absorption region. There are two possible ways to realize this goal; one is to increase the drift-velocity of photo-generated carriers and the other is to directly downscale the depletion layer thickness. By eliminating the slow hole-transport in the UTC-PD, the effective caerrier drift-velocity is improved and excellent high-speed and high-power perfromance has been demonstarted. By further increasing the electron drift-velocity in UTC-PD, the NBUTC-PD structure has demonsatretd superior saturation-current bandwidth product with high responsivity. Although to directly downscale the depletion layer thickness is the most straightforward way to improve high-power performance of PD, its RC-limited bandwidth and responsivity performance are usually sacrificed. In order to release the tarde-off among depletion layer thickness, RC-limimited bandwidth, and responsivity performance of PDs, STR-PD and PDP strcuctures have been demonstarted. By inserting a p-type region and a material with extermely short lifetime (<1ps) in the absorption region of PDP and STR-PD, respectively, superior high-power performance of both structure to traditional p-i-n PDs have both been demonstarted.

In the third part of this chapter, we disscussed the application of one kind of high-power PD: NBUTC-PD, and photonic transmitter to the RoF communication system. By use of the bias modualtion technique on NBUTC-PD, the QPSK and BPSK wirless data transmission at 100GHz frequency has been successfully demonstarted.

6. References

[1]A. Hirata, T. Kosugi, H. Takahashi, R. Yamaguchi, F. Nakajima, T. Furuta, H. Ito, H. Sugahara, Y. Sato, and T. Nagatsuma, "120-GHz-Band Millimeter-Wave Photonic Wireless Link for 10-Gb/s Data Transmission," *IEEE Trans. Microwave Theory Tech.*, vol. 54, pp. 1937-1944, May. 2006.

[2]A. Hirata, H. Ishii, and T. Nagatsuma, "Design and Characterization of a 120-GHz Millimeter-Wave Antenna for Integrated Photonic Transmitters," *IEEE Trans. Microwave Theory Tech.*, vol. 49, pp. 2157-2162, Nov. 2001.

[3]A. J. Seeds and K. J. Williams, "Microwave Photonics," *J. of Lightwave Technol.*, vol. 24, pp. 4628-4641, Dec, 2006.

[4]K. Kato, "Ultrawide-Band/High-Frequency Photodetectors," *IEEE Trans. Microwave Theory Tech.,* vol. 47, pp. 1265-1281, Jul., 1999.

[5]H. Ito, S. Kodama, Y. Muramoto, T. Furuta, T. Nagatsuma, T. Ishibashi, "High -Speed and High-Output InP-InGaAs Unitraveling-Carrier Photodiodes," *IEEE J. of Sel. Topics in Quantum Electronics,* vol. 10, pp. 709-727, Jul., 2004.

[6]T. H. Stievater and K. J. Williams, "Thermally Induced Nonlinearities in High-Speed p-i-n Photodetectors," *IEEE Photon. Technol. Lett,* vol. 16, pp. 239-241, Jan., 2004.

[7]F. Xia, J. K. Thomson, M. R. Gokhale, P. V. Studenkov, J. Wei, W. Lin, and S. R. Forrest, "A asymmetric twin-waveguide high-bandwidth photodiode using a lateral taper coupler," *IEEE Photon. Technol. Lett.,* vol. 13, pp. 845-847, Aug., 2001.

[8]S. Demiguel, N. Li, X. Li, X. Zheng, J. Kim, J. C. Campbell, H. Lu, and A. Anselm, "Very High-Responsivity Evanescently Coupled Photodiodes Integrating a Short Planar Multimode Waveguide for High-Speed Applications," *IEEE Photon. Technol. Lett.*, vol. 15, pp.1761-1763, Dec., 2003.

[9]Y.-S. Wu, J.-W. Shi, J.-Y. Wu, F.-H. Huang, Y.-J. Chan, Y.-L. Huang, and R. Xuan "High Performance Evanescently Edge Coupled Photodiodes with Partially p-Doped Photo-absorption Layer at 1.55μm Wavelength" *IEEE Photon. Tech. Lett* vol. **17**, pp.878-880, April, 2005.

[10]X. Li, N. Li, S. Demiguel, X. Zheng, J. C. Campbell, H. H. Tan, and C. Jagadish, "A Partially Depleted Absorber Photodiode With Graded Doping Injection Regions," *IEEE Photon. Technol. Lett.*, vol. 16, pp.2326-2328, Oct., 2004.

[11]J.-W. Shi, H.-C. Hsu, F.-H. Huang, W.-S. Liu, J.-I. Chyi, Ja-Yu Lu, Chi-Kuang Sun, and Ci-Liang Pan, "Separated-Transport-Recombination p-i-n Photodiode for High-speed and High-power Performance" *IEEE Photon. Technol. Lett,* vol. 17, pp. 1722-1724, Aug., 2005.

[12]L. Y. Lin, M. C. Wu, T. Itoh, T. A. Vang, R. E. Muller, D. L. Sivco, and A. Y. Cho, "High-power High-speed Photodetectors Design, Analysis, and Experiment Demonstration," *IEEE Trans. Microwave Theory Tech.,* vol. 45, pp. 1320-1331, Aug., 1997.

[13]M. Achouche, V. Magnin, J. Harari, F. Lelarge, E. Derouin, C. Jany, D. Carpentier, F. Blache, and D. Decoster, "High performance evanescent edge coupled waveguide unitraveling-carrier photodiodes for >40-Gb/s optical receivers," *IEEE Photon. Technol. Lett.,* vol. 16, pp. 584-586, Feb., 2004.

[14]W.-Y. Chiu, J.-W. Shi, W.-K. Wang, Y.-S. Wu, Y.-J. Chan, Y.-L. Huang, and R. Xuan, "Leaky-Wave Photodiodes with a Partially p-Doped Absorption Layer and a Distributed-Bragg-Reflector (DBR) for High-Power and High-Bandwidth-

Responsivity Product Performance" *IEEE Photon. Technol. Lett.,* vol. 18, pp. 1323-1325, June, 2006.

[15]Y.-S. Wu, J.-W. Shi, P.-H. Chiu, and Wei Lin "High-Performance Dual-Step Evanescently-Coupled Uni-Traveling-Carrier Photodiodes" *IEEE Photon. Technol. Lett.,* vol. 19, pp. 1682-1684, 2007.

[16]S. Demiguel, X. Li, N. Li, H. Chan, J. C. Campbell, J. Wei and A. Anselm, "High-Responsivity High-speed and High-power Partially Depleted Absorber Waveguide Photodiodes with Relaxed Coupling Tolerance" in *Proc. OFC 2005,* vol. 3, pp.WQ2-1-WQ2-3.

[17]A. Beling, J. C. Campbell, H.-G. Bach, G. G. Mekonnen, and D. Schmidt, "Parallel-Fed Traveling Wave Photodetector for >100-GHz Applications," *J. of Lightwave Technol.*, vol. 26, pp. 16-20, Jan., 2008.

[18]Y.-S. Wu, J.-W. Shi, and P.-H. Chiu "Analytical Modeling of a High-Performance Near-Ballistic Uni-Traveling-Carrier Photodiode at a 1.55μm Wavelength," *IEEE Photon. Technol. Lett.,* vol. 18, pp. 938-940, April, 2006.

[19]E. Lach and K. Schuh, "Recent Advances in Ultrahigh Bit Rate ETDM Transmission Systems," *J. Lightwave Technol.,* vol. 24, pp. 4455-4467, Dec., 2006.

[20]A. Beling, Heinz-Gunter Bach, G. G. Mekonnen, R. Kunkel, and D. Schmidt, "Miniaturized waveguide-integrated p-i-n photodetector with 120-GHz bandwidth and high responsivity," *IEEE Photon. Technol. Lett.,* vol. 17, pp. 2152-2154, Oct., 2005.

[21]Y. Hirota, T. Hirono, T. Ishibashi, and H. Ito, "Traveling-Wave Photodetector for 1.55μm Wavelength Fabricated with Uni-Taveling-Carrier Photodiodes" *Appl. Phys. Lett.,* vol. 78, pp. 3767-3769, 2001.

[22]J.-W. Shi, C.-Y. Wu, Y.-S. Wu, P.-H. Chiu, and C.-C. Hong, High-Speed, High-Responsivity, and High-Power Performance of Near- Ballistic Uni-Traveling-Carrier Photodiode at 1.55μm Wavelength,"*IEEE Photon. Technol. Lett.,* vol. 17, pp. 1929-1931, Sep., 2005.

[23]Y.-S. Wu, and J.-W. Shi, "Dynamic Analysis of High-Power and High-Speed Near-Ballistic Unitraveling Carrier Photodiodes at W-Band," *IEEE Photon. Technol. Lett.*, vol. 20, pp. 1160-1162, July, 200

[24]T. Ishibashi and Y. Yamauchi, "A Possible Near-Ballistic Collection in an AlGaAs/GaAs HBT with a Modified Collector Structure," *IEEE Trans. on Electron Devices,* vol. 35, pp. 401-404, April, 1988.

[25]T. Ishibashi, "Nonequilibrium Electron Transport HBTs," *IEEE Trans. on Electron Devices,* vol. 48, pp. 2595-2604, Nov., 2001.

[26]G. Wang, T. Tokumitsu, I. Hanawa, K. Sato, and M. Kobayashi, "A Time-Delay Equivalent-Circuit Model of Ultrafast p-i-n Photodiodes", *IEEE Trans. Microwave Theory Tech.,* vol. 51, pp. 1227-1233, April, 2003.

[27]N. Li, H. Chen, N. Duan, M. Liu, S. Demiguel, R. Sidhu, A. L. Holmes, Jr., and J. C. Campbell, "High Power Photodiode Wafer Bonded to Si Using Au With Improved Responsivity and Output Power" *IEEE Photon. Technol. Lett,* vol. 18, pp. 2526-2528, Dec., 2006.

[28]N. Li, X. Li, S. Demiguel, X. Zheng, J. C. Campbell, D. A. Tulchinsky, K. J. Williams, T. D. Isshiki, G. S. Kinsey, and R. Sudharsansan, "High-Saturation-Current Charge-Compensated InGaAs-InP Uni-Traveling-Carrier Photodiode," *IEEE Photon. Technol. Lett.*, vol. 16, Mar., pp.864-866, 2004.

[29]Y.-S. Wu, J.-W. Shi, J.-Y. Wu, F.-H. Huang, Y.-J. Chan, Y.-L. Huang, and R. Xuan, "Design and Demonstration of High-Power and High-Speed Evanescently Coupled Photodiodes with Partially p-Doped Photo-absorption Layer" *Conference on Laser and Electro-Optics (CLEO/QELS'2005)*, USA, OSA Technical Digest, CMGG1, 2005.

[30]S. Gupta, J. F. Whitaker, and G. A. Mourou, "Ultrafast Carrier Dynamics in III-V Semiconductors Grown by Molecular-Beam Epitaxy at Very Low Substrate Temperatures," *IEEE J. of Quantum Electronics,* vol. 28, pp.2464-2472, Oct., 1992.

[31]Y. J. Chiu, S. B. Fleischer, and J. E. Bowers, "High-Speed Low-Temperature-Grown GaAs p-i-n Traveling-Wave Photodetector," *IEEE Photon. Technol. Lett.*, vol. 10, pp.1012-1014, July, 1998.

[32]N. Zamdmer, Qing Hu, K. A. Mclntosh, and S. Verghese, " Increase in Response Time of Low-Temeprature-Grown GaAs Photoconductive Switches at High Voltage Bias" *Appl. Phys. Lett.,* vol. 75, pp. 2313-2315, Oct., 1999.

[33]Yu-Tai Li, J.-W. Shi, Ci-Ling Pan, C.-H. Chiu, W.- S. Liu, Nan-Wei Chen, C.-K. Sun, and J.-I. Chyi, "Sub-THz Photonic-Transmitters Based on Separated-Transport-Recombination Photodiodes and a Micromachined Slot Antenna" *IEEE Photon. Technol. Lett.,* vol. 19, pp. 840-842, June, 2007.

[34]Yu-Tai Li, J.-W. Shi, C.-Y. Huang, N.-W. Chen, S.-H. Chen, J.-I. Chyi, and Ci-Ling Pan, "Characterization of Sub-THz Photonic-Transmitters Based on GaAs/AlGaAs Uni-Traveling Carrier Photodiodes and Substrate-Removed Broadband Antennas for Impulse-Radio Communication," *IEEE Photon. Technol. Lett.,* vol. 20, pp.1342-1344, Aug., 2008.

[35]Y. S. Wu, N. W. Chen, and J. W. Shi, "A W-Band Photonic Transmitter/Mixer Based on High-Power Near-Ballistic Uni-Traveling-Carrier Photodiode (NBUTC-PD)," *IEEE Photon. Technol. Lett.*, vol. 20, pp. 1799-1801, Nov., 2008.

[36]M. Tsuchiya, and T. Hosida, "Nonlinear Photodetection Scheme and Its System Applications to Fiber-Optic Millimeter-Wave Wireless Down-Links" *IEEE Trans. Microwave Theory Tech.,* vol. 47, 1999.

[37]H. Fushimi, T. Furuta, T. Ishibashi, and H. Ito, "Photoresponse Nonlinearity of a Uni-Traveling-Carrier Photodiode and Its Application to Optoelectronic Millimeter-Wave Mixing in 60GHz Band," *Jpn. J. Appl. Phys.,* vol. 43, pp. L966-L968, July, 2004.

[38]H.-C. Chien, A. Chowdhury, Z. Jai, Y.-T. Hsueh, and G.-K. Chang, "Long-Reach 60-GHz Mm-Wave Optical-Wireless Access Network Using Remote Signal Regeneration and Upconversion," in *Proc.* ECOC 2008, *Brussels,* Belgium, Germany, Sep., 2008, vol. 2, pp. 137-138.

[39]N. Kaneda, W. R. Deal, Y. Qian, R. Waterhouse, and T. Itoh, "A broadband planar quasi-Yagi antenna," *IEEE Trans. on Antennas and Propagation*, vol. 50, pp. 1158-1160, Aug., 2002.

[40]G. M. Rebeiz, "Millimeter-wave and terahertz integrated circuit antennas," *Proceedings of IEEE,* vol. 80, pp. 1748-1770, 1992.

[41]Y.-C. Liang and N.-W. Chen, "An ultra-broadband coplanar waveguide-fed circular monopole antenna," *EuCAP 2007*, Edinburgh, UK, Nov., 2007.

[42]J.-W. Shi, Y.-S. Wu, and Y.-S. Lin, "Near-Ballistic Uni-Traveling-Carrier Photodiode Based V-band Optoelectronic Mixers with Internal Up-Conversion-Gain, Wide Modulation Bandwidth, and Very High Operation Current Performance," *IEEE Photon. Technol. Lett.*, vol. 20, pp. 939-941, June, 2008.

[43]A. Hirata, T. Furuta, H. Ito, and T. Nagatsuma, "10-Gb/s Millimeter-Wave Signal Generation Using Photodiode Bias Modulation," *J. of Lightwave Technol.*, vol. 24, pp. 1725–1731, April. 2006.

[44]P. T. Shih, C. T. Lin, W. J. Jiang, E. Z. Wong, J. Chen, S. Chi, Y. -S. Wu, F. -M. Kuo, N. -W. Chen, and J. -W. Shi, "W-Band Vector Signal Generation via Optical Millimeter-Wave Generation and Direct Modulation of NBUTC-PD," *Proc. OFC 2009, San Diego*, CA, USA, March, 2009, pp. OWP4.

Optical Fiber New Developments

Edited by Christophe Lethien

ISBN 978-953-7619-50-3

Hard cover, 586 pages

Publisher InTech

Published online 01, December, 2009

Published in print edition December, 2009

The optical fibre technology is one of the hop topics developed in the beginning of the 21th century and could substantially benefit applications dealing with lighting, sensing and communication systems. Many improvements have been made in the past years to reduce the fibre attenuation and to improve the fibre performance. Nowadays, new applications have been developed over the scientific community and this book fits this paradigm. It summarizes the current status of know-how in optical fibre applications and represents a further source of information dealing with two main topics: the development of fibre optics sensors, and the application of optical fibre for telecommunication systems.

How to reference

In order to correctly reference this scholarly work, feel free to copy and paste the following:

J.-W. Shi, F.-M. Kuo and Y.-S. Wu (2009). High-Speed, High-Power, and High Responsivity Photodiode for Radio-Over-Fiber (ROF) Communication, Optical Fiber New Developments, Christophe Lethien (Ed.), ISBN: 978-953-7619-50-3, InTech, Available from: http://www.intechopen.com/books/optical-fiber-new-developments/high-speed-high-power-and-high-responsivity-photodiode-for-radio-over-fiber-rof-communication

INTECH
open science | open minds

InTech Europe
University Campus STeP Ri
Slavka Krautzeka 83/A
51000 Rijeka, Croatia
Phone: +385 (51) 770 447
Fax: +385 (51) 686 166
www.intechopen.com

InTech China
Unit 405, Office Block, Hotel Equatorial Shanghai
No.65, Yan An Road (West), Shanghai, 200040, China
中国上海市延安西路65号上海国际贵都大饭店办公楼405单元
Phone: +86-21-62489820
Fax: +86-21-62489821

IntechOpen